

Analysis of process-induced deformations and residual stresses in curved composite parts considering transverse shear stress and thickness stretching

*Original*

Analysis of process-induced deformations and residual stresses in curved composite parts considering transverse shear stress and thickness stretching / Zappino, E.; Zobeiry, N.; Petrolo, M.; Vaziri, R.; Carrera, E.; Poursartip, A.. - In: COMPOSITE STRUCTURES. - ISSN 0263-8223. - STAMPA. - 241:(2020). [10.1016/j.compstruct.2020.112057]

*Availability:*

This version is available at: 11583/2799892 since: 2020-03-03T08:03:52Z

*Publisher:*

Elsevier

*Published*

DOI:10.1016/j.compstruct.2020.112057

*Terms of use:*

This article is made available under terms and conditions as specified in the corresponding bibliographic description in the repository

*Publisher copyright*

Elsevier postprint/Author's Accepted Manuscript

© 2020. This manuscript version is made available under the CC-BY-NC-ND 4.0 license  
<http://creativecommons.org/licenses/by-nc-nd/4.0/>. The final authenticated version is available online at:  
<http://dx.doi.org/10.1016/j.compstruct.2020.112057>

(Article begins on next page)

# Analysis of process-induced deformations and residual stresses in curved composite parts considering transverse shear stress and thickness stretching

E. Zappino<sup>a,d</sup>, N. Zobeiry<sup>b</sup>, M. Petrolo<sup>a</sup>, R. Vaziri<sup>c</sup>, E. Carrera<sup>a</sup>, A. Poursartip<sup>c</sup>

<sup>a</sup>*MUL<sup>2</sup> Group, Department of Mechanical and Aerospace Engineering, Politecnico di Torino, Corso Duca degli Abruzzi 24, 10129 Torino, Italy.*

<sup>b</sup>*Materials Science & Engineering Department, University of Washington, 302 Roberts Hall, Seattle, WA, USA*

<sup>c</sup>*Composites Group, Departments of Civil Engineering and Materials Engineering, The University of British Columbia, Vancouver, BC, V6T 1Z4, Canada*

<sup>d</sup>*Corresponding Author, email: enrico.zappino@polito.it*

---

## Abstract

A computationally efficient modeling approach for the accurate evaluation of process-induced deformations and residual stresses in composite parts is presented. A family of refined one-dimensional kinematic models, developed in the framework of the Carrera Unified Formulation, has been used to predict the accurate through-thickness deformation of layered structures during the manufacturing process. The composite material curing phase has been simulated exploiting the capabilities of the software RAVEN. A cure hardening instantaneously linear elastic model has been used. A benchmark based on an L-shaped component has been selected to compare the results obtained using different computational approaches. A closed-form solution, the present refined one-dimensional models and classical solid models, have been considered. The effects of the modeling approach on the prediction of the spring-in angle and on the residual stress field have been evaluated and discussed. The results demonstrate that the use of refined kinematic models can lead to a high-fidelity description of the problem and a quasi-3D accuracy while reducing the computational cost with respect to classical FEM approaches. The through-thickness effects have been predicted with a high level of accuracy and the use of layer-wise models has led to an accurate description of the stress field, including the transverse shear stresses.

*Keywords:* CUF, one-dimensional model, virtual manufacturing, residual stress, process-induced deformations

---

## 1. Introduction

Composite materials are widely used in high-performance structural applications due to their superior specific mechanical properties. The ability to manufacture complex monolithic struc-

tures using these materials makes them attractive for many applications.

During the manufacturing process, composite parts are commonly subjected to high pressure and temperature cycles during which thermal/curing-induced free-strains are formed [1]. Mismatch of these free strains at various scales, coupled with the evolution of mechanical properties, leads to formation of residual stresses and consequently dimensional changes in the cured composite part. The mismatch occurs at the micro-level between constituents (i.e. fiber and matrix), at the meso-level between plies with different orientations, and at the macro-level between the part and the tool via friction and other geometrical constraints [2]. These manufacturing-induced dimensional changes may reduce mechanical performance and pose significant challenges during the assembling of large and complex parts. Further complexities arise when considering part orthotropic properties and tool-part interaction in configured geometries such as C-shape and L-shape [3, 4]. For typical laminate layups such as cross-ply or quasi-isotropic, in-plane free strains are negligible compared to through-thickness free strains. As a result, around curved corners, this results in formation of residual stresses leading to dimensional changes [2]. At the early stages of curing and while the through-thickness shear modulus is much smaller than the effective bending stiffness of the laminate, residual stresses are mostly released via transverse shear deformation. As the shear modulus is evolved, mismatch of free-strains results in formation of residual stresses. This processing-induced residual stress is partly released upon demoulding which in turn results in bending deformation including spring-in angle and warpage. This is shown schematically in Fig. 1.

In the past decade, many studies have been conducted to analyze and predict dimensional changes in composites and metals either through simplified analytical solutions or high fidelity finite element (FE) simulations [5, 6, 7, 8, 9]. Often, to obtain analytical solutions, simplified assumptions are made on the behavior of the material or the underlying physics governing the problem. Initially, simple mechanics-based models were developed while neglecting the effect of transverse shear [10, 11]. These were obtained based on the mismatch between the in-plane and through-thickness free-strains resulting in laminate bending deformation. Wisnom et al. [12] included the effect of transverse shear in curved beams using a shear-lag approach while simplifying the evolution of material properties to rubbery and glassy regimes. In a similar approach, Arafath et al. [13] included the shear effect in a curved beam while considering more accurate representation of material properties using a pseudo-viscoelastic Cure Hardening Instantaneous Linear Elastic (CHILE) constitutive model [14]. Takagaki et al. [15, 16] expanded the analytical solution to C-shape and L-shape geometries while using the CHILE model, and

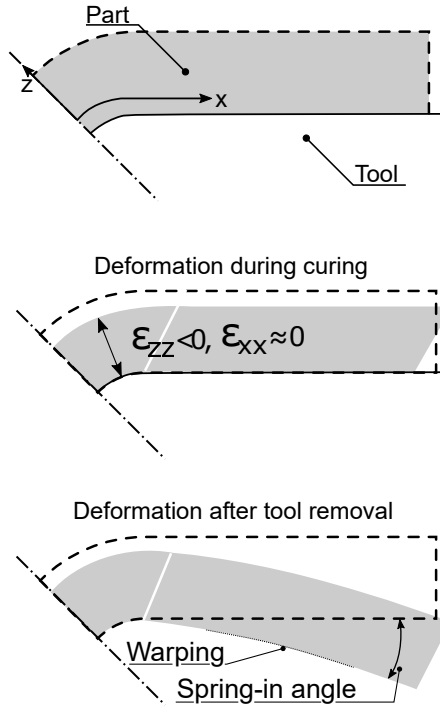


Figure 1: Schematics of residual spring-in angle and warpage in curved composite parts after curing process and subsequent tool removal.

Ding et al. focused on the inclusion and evaluation of the flange length [17]. In terms of numerical simulations, 2D/3D analyses are widely performed (e.g. [7]) using FE commercial software packages such as COMPRO [18]. Often in these codes, various constitutive models such as pseudo-viscoelastic, visco-elastic or thermo-viscoelastic [19], are available for a more complex representation of the material behavior during processing. Aside from predicting the spring-in angle, these tools can be used to mitigate the process-induced deformations using tool-geometry compensation [20].

Numerical models, such as those based on FE methods [21], have been routinely used to simulate the curing process of polymeric composites, including micromechanics [22, 23], nonlinear analyses [24]. Recently, advances have been made towards the reliable modeling of complex aerospace components [25], and the inclusion of viscoelastic effects [26, 27]. The classical structural formulations, e.g., beam and plate elements, necessitate the use of three-dimensional continuum elements with a considerable increase of the computational costs. The present work aims to exploit the capabilities of a refined kinematic one-dimensional model [28, 29], developed within the framework of the Carrera Unified Formulation (CUF) [30], to obtain an accurate prediction

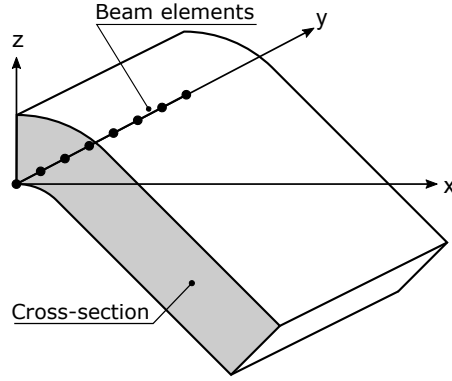


Figure 2: Reference coordinate system.

of the residual deformations and stresses due to the curing process.

The structural model has been extended to the analysis of the curing process. The evolution of the material properties during the curing process are evaluated using the software RAVEN [31] and the process analysis is carried out using the CHILE model [14]. The tool removal phase has also been taken into account to evaluate the final shape and the residual stresses at the end of the manufacturing process.

This paper is organized as follows: Section 2 presents the structural modeling and FE formulation, while Section 3 describes the curing model, Section 4 presents the material properties, and the results and conclusions are presented in Sections 5 and 6, respectively.

## 2. One-dimensional refined kinematic model

A refined one-dimensional kinematic model has been used in the present work. The governing equations have been derived within the CUF framework. The main features of the present model are introduced in this section. More details can be found in the book by Carrera *et al.*[30].

The reference coordinate system adopted is shown in Fig. 2. The coordinate  $y$  is aligned with the axis of the composite part while  $x$  and  $z$  axes lay on the cross-section. The displacement vector is written as:

$$\mathbf{u}^T = (u_x, u_y, u_z) \quad (1)$$

where  $u_x$ ,  $u_y$  and  $u_z$  are the three displacement components. The strain and stress vectors are

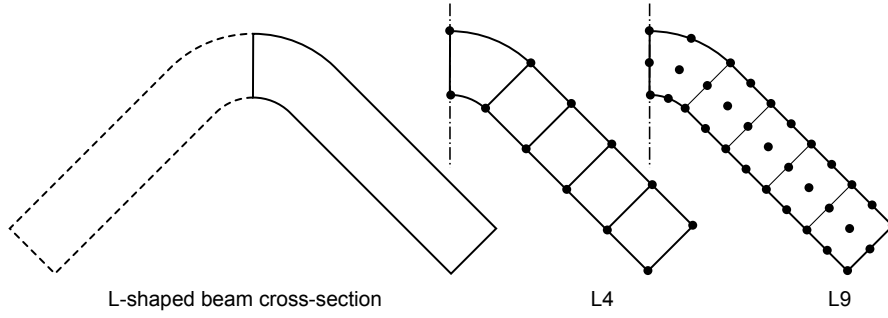


Figure 3: Examples of cross-sectional meshes using linear (L4) and quadratic (L9) elements.

defined as:

$$\boldsymbol{\varepsilon}^T = (\varepsilon_{xx}, \varepsilon_{yy}, \varepsilon_{zz}, \varepsilon_{xz}, \varepsilon_{yz}, \varepsilon_{xy}), \quad (2)$$

$$\boldsymbol{\sigma}^T = (\sigma_{xx}, \sigma_{yy}, \sigma_{zz}, \sigma_{xz}, \sigma_{yz}, \sigma_{xy}). \quad (3)$$

The relation between strains and displacements can be written using the geometrical equation:

$$\boldsymbol{\varepsilon} = \mathbf{D}\mathbf{u}, \quad (4)$$

where  $\mathbf{D}$  is a matrix of linear differential operators. Adopting Hooke's law allows the relation between stresses and strains to be written as:

$$\boldsymbol{\sigma} = \mathbf{C}\boldsymbol{\varepsilon}, \quad (5)$$

where  $\mathbf{C}$  is the matrix of stiffness coefficients of the material.

### 2.1. Kinematic model

The refined one-dimensional kinematic model adopted here assumes the cross-sectional displacement field to be written as an expansion of two-dimensional Lagrange functions. Figure 3 shows an example of the cross-sectional discretizations. The displacement field can be written in a general form as:

$$\mathbf{u} = \mathbf{u}_\tau(y)F_\tau(x, z), \quad \tau = 1 \dots M. \quad (6)$$

where  $F_\tau(x, z)$  is the expansion function over the cross-section,  $\mathbf{u}_\tau(y)$  is the unknown displacement vector along the beam axis, and  $M$  is the number of terms in the expansion functions

$F_\tau(x, z)$ . If the cross-section is described with a four-node Lagrange element (L4) the displacement field assumes the following form:

$$\mathbf{u} = \mathbf{u}_1 L_1 + \mathbf{u}_2 L_2 + \mathbf{u}_3 L_3 + \mathbf{u}_4 L_4. \quad (7)$$

The expansion functions have been denoted with  $L$  instead of  $F$  to highlight that they are Lagrange polynomials. When more than one element is used, the cross-sectional compatibility of the displacements can be imposed by a proper standard assembly procedure.

The FE model approximates the axial unknowns  $\mathbf{u}_\tau(y)$  using the one-dimensional shape functions,  $N_i$ . The displacement field assumes the form:

$$\mathbf{u} = \mathbf{u}_{i\tau} N_i(y) F_\tau(x, z), \quad \tau = 1 \dots M; \quad i = 1 \dots N_n, \quad (8)$$

where  $N_i$  are the shape functions introduced by the FE model,  $N_n$  is the number of nodes of the element and  $\mathbf{u}_{i\tau}$  are the nodal unknowns.

## 2.2. Governing equations

The governing equations can be derived using the Principle of Virtual Displacements (PVD) which assumes the following form in the static case:

$$\delta L_{int} = \delta L_{ext} \quad (9)$$

where  $L_{int}$  stands for the strain energy,  $L_{ext}$  is the work of the external loads and  $\delta$  denotes the virtual variation. The variation of the strain energy can be written as:

$$\delta L_{int} = \int_V \delta \boldsymbol{\varepsilon}^T \boldsymbol{\sigma} dV \quad (10)$$

By introducing the constitutive equations and the geometrical relations, respectively, and introducing the displacement field given in Eq. 8, Eq. 10 becomes:

$$\delta L_{int} = \delta \mathbf{u}_{sj}^T \int_V \left[ N_j F_s \mathbf{D}^T \mathbf{C} \mathbf{D} F_\tau N_i \right] dV \mathbf{u}_{\tau i} \quad (11)$$

$$= \delta \mathbf{u}_{sj}^T \mathbf{k}^{ij\tau s} \mathbf{u}_{\tau i} \quad (12)$$

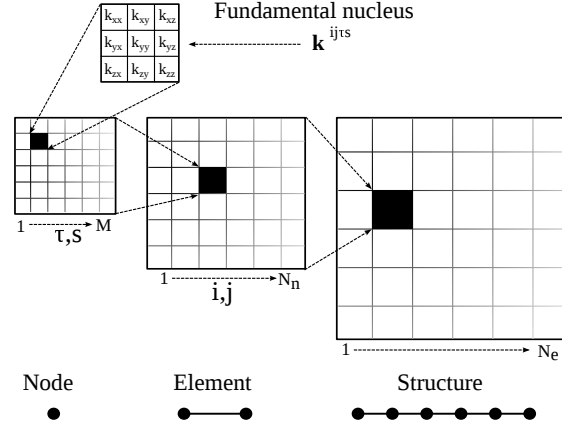


Figure 4: Stiffness matrix assembly procedure.

where  $\mathbf{k}^{ij\tau s}$  is the stiffness matrix expressed in the form of a *fundamental nucleus* that is a  $3 \times 3$  matrix with an invariant form,  $\mathbf{u}_{\tau i}$  is the vector of the nodal unknowns and  $\delta \mathbf{u}_{s j}$  is its first variation.

The external loads, in the case of the curing process simulation, are body forces that are generated from the thermal field and the chemical shrinkage. The present paper considers both of these loads as an input of the analysis and are separately computed using RAVEN. The temperature increment is defined as  $\Delta T$  while the strain vector due to the chemical shrinkage is  $\varepsilon_s$ . The variation of the external work is written as:

$$\delta L_{ext} = \int_V \delta \boldsymbol{\varepsilon}^T \mathbf{C} \boldsymbol{\beta} \Delta T dV + \int_V \delta \boldsymbol{\varepsilon}^T \mathbf{C} \boldsymbol{\varepsilon}_s dV \quad (13)$$

where  $\boldsymbol{\beta}$  is the vector of the coefficients of thermal expansion. Considering the displacement field formulation introduced in Eq. 8, Eq. 13 becomes:

$$\delta L_{ext} = \delta \mathbf{u}_{s j}^T \int_V N_j F_s \mathbf{D}^T \mathbf{C} (\boldsymbol{\beta} \Delta T + \boldsymbol{\varepsilon}_s) dV = \delta \mathbf{u}_{s j}^T \mathbf{f}^{j s}, \quad (14)$$

where  $\mathbf{f}^{j s}$  is a column vector with three components and is referred to as the fundamental nucleus of the load vector. The fundamental nucleus of the stiffness matrix and of the load vector can be easily assembled into the global stiffness matrix,  $\mathbf{K}$ , and load vector,  $\mathbf{F}$ , via an iterative procedure over the indexes  $i, j, \tau$  and  $s$  (see Fig. 4).



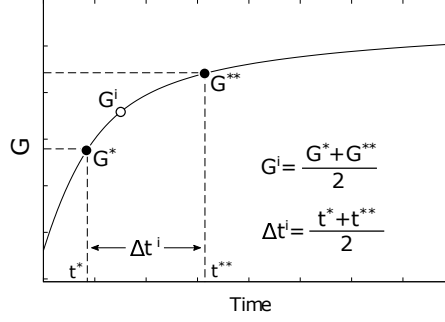


Figure 5: Material property at the  $i$ -th time step.

### 3. Curing process analysis

The simulation of the curing process has been performed using the CHILE constitutive model. This approach, exhaustively presented by Johnston *et al.*[14], assumes the solution at the end of the curing process as being the summation of the instantaneous elastic solutions in a discrete number,  $N_\alpha$ , of time steps. The properties of the material are evaluated as the average at each step. Figure 5 shows how the shear modulus is defined at the  $i$ -th time step. The increment of the shrinkage and thermal strains,  $\Delta\varepsilon_s^i$  and  $\Delta\varepsilon_T^i$ , respectively, are used as external loads at the  $i$ -th time step. Figure 6 shows the flowchart of the solution procedure. At first, the material properties and the load variations are defined at the  $i$ -th step, then, a static linear problem can be solved:

$$\mathbf{K}^i \Delta \mathbf{u}^i = \Delta \mathbf{F}^i \quad (15)$$

where  $\mathbf{K}^i$  is the stiffness matrix of the whole model (part, tool and the interfacial shear layer) evaluated at the  $i$ -th time step.  $\Delta \mathbf{F}^i$  is the load vector at the  $i$ -th step and  $\Delta \mathbf{u}^i$  is the solution increment.

The stress and strain increments can be readily evaluated by means of the geometrical relations and the Hooke's law:

$$\Delta \varepsilon^i = \mathbf{D} \Delta \mathbf{u}^i; \quad \Delta \sigma^i = \mathbf{C}^i \Delta \varepsilon^i \quad (16)$$

The interfacial tool/part forces can be obtained by integrating the stresses at the interface, as proposed in [14]. In order to avoid a further integration procedure, the interface forces can also be obtained by exploiting the properties of the stiffness matrix that has been already calculated in the previous steps. The stiffness matrix,  $\mathbf{K}^i$ , can be considered as the sum of many contributions,

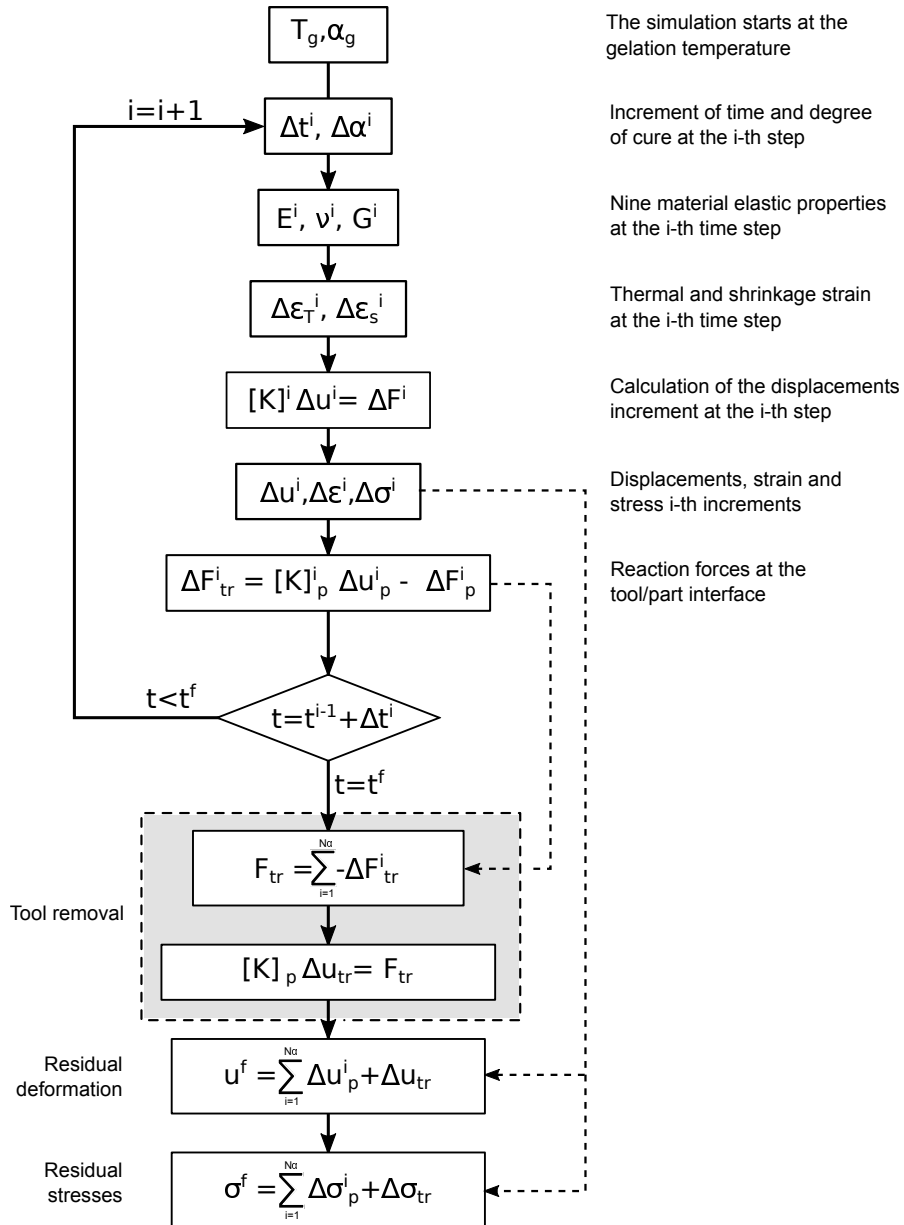


Figure 6: Curing analysis solution algorithm.

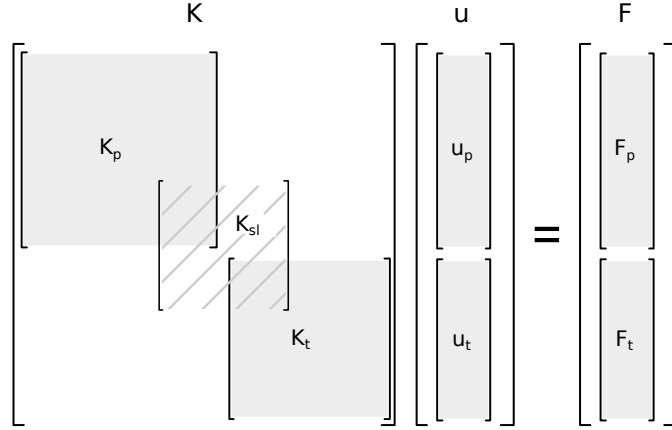


Figure 7: Partitioning of the total stiffness matrix.

as shown in Fig. 7.  $\mathbf{K}_p^i$  is the matrix related to the composite part,  $\mathbf{K}_t^i$  is the stiffness coming from the tool and  $\mathbf{K}_{sl}^i$  is the stiffness contribution due to the interface model, in this case a shear layer. The same partition can be applied to the displacement and force vectors; these contributions have not been reported in Fig. 7. The forces acting on the composite part,  $\Delta \bar{\mathbf{F}}_p^i$ , can be calculated as:

$$\Delta \bar{\mathbf{F}}_p^i = \mathbf{K}_p^i \Delta \mathbf{u}_p^i \quad (17)$$

The vector  $\Delta \bar{\mathbf{F}}_p^i$  includes the external force due to the shrinkage, the thermal loads, and the interface forces since  $\mathbf{K}_p^i$  does not include the stiffness of the tool and the shear layer, that is, a certain amount of internal force is not balanced at the interface. The interface force vector at the  $i$ -th time step due to the tool removal,  $\Delta \mathbf{F}_{tr}^i$ , can be finally obtained as:

$$\Delta \mathbf{F}_{tr}^i = \Delta \bar{\mathbf{F}}_p^i - \Delta \mathbf{F}_p^i \quad (18)$$

Once the curing simulation is concluded, it is possible to proceed with the evaluation of the final process-induced deformations. The total amount of forces that the tool applies on the composite part,  $\mathbf{F}_{tr}$ , is given by:

$$\mathbf{F}_{tr} = \sum_{i=1}^{N_\alpha} \Delta \mathbf{F}_{tr}^i \quad (19)$$

where  $N_\alpha$  is the number of time steps used in the simulation.

The increment of the displacements that appears as a consequence of the tool removal can

thus be calculated by solving the following linear system:

$$\mathbf{K}_p \Delta \mathbf{u}_{tr} = \mathbf{F}_{tr} \quad (20)$$

$\boldsymbol{\varepsilon}_{tr}$  and  $\boldsymbol{\sigma}_{tr}$  can be obtained using Eqs. 4 and 5. The total residual displacements, deformations and stresses due to the curing process and the tool removal can now be calculated as:

$$\mathbf{u}^f = \sum_{i=1}^{N_\alpha} \Delta \mathbf{u}_p^i + \Delta \mathbf{u}_{tr} \quad (21)$$

$$\boldsymbol{\varepsilon}^f = \sum_{i=1}^{N_\alpha} \Delta \boldsymbol{\varepsilon}_p^i + \Delta \boldsymbol{\varepsilon}_{tr} \quad (22)$$

$$\boldsymbol{\sigma}^f = \sum_{i=1}^{N_\alpha} \Delta \boldsymbol{\sigma}_p^i + \Delta \boldsymbol{\sigma}_{tr} \quad (23)$$

#### 4. Material

The composite material used in this study was AS4/8552 unidirectional prepreg by Hexcel [32]. The prepreg consists of about 35% (by weight) 8552 epoxy resin system and 65% AS4 HexTow carbon fibers with an areal weight of 190  $\frac{gr}{m^2}$  [33]. The cured ply thickness is about 0.19 mm. Curing process and evolution of mechanical properties/free-strains were simulated using the RAVEN software [31]. Cure kinetics model and data published by National Center for Advanced Materials Performance (NCAMP) [34, 35] were implemented in RAVEN and used for cure simulation. The 8552 free-strains from the work by Mobuchon et al. [36] were implemented in RAVEN and used for the current simulations.

For curing, a one-hold cycle with a heating rate of 1 °C/min and a hold temperature of 180 °C for 2 hours was used as shown in Fig. 8. Evolution of curing as predicted by RAVEN is also shown in Fig. 8.

The evolution of mechanical properties of the AS4/8552 lamina as predicted by RAVEN are shown Figs. 9a, b and c. This includes the evolution of the Young's moduli, the shear moduli and the Poisson's ratios. Figures 10a and b report the evolution of cure shrinkage and thermal expansion coefficients during curing. For all properties, the values are only reported for a degree of cure higher than 0.54 for which gelation occurs. All the lamina-level properties are reported in Appendix B.

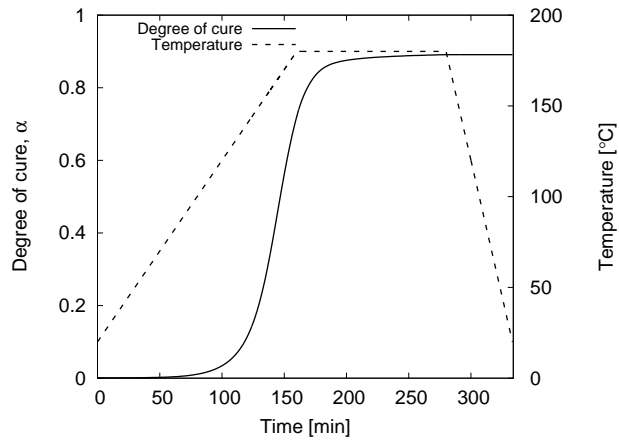


Figure 8: Curing Cycle.

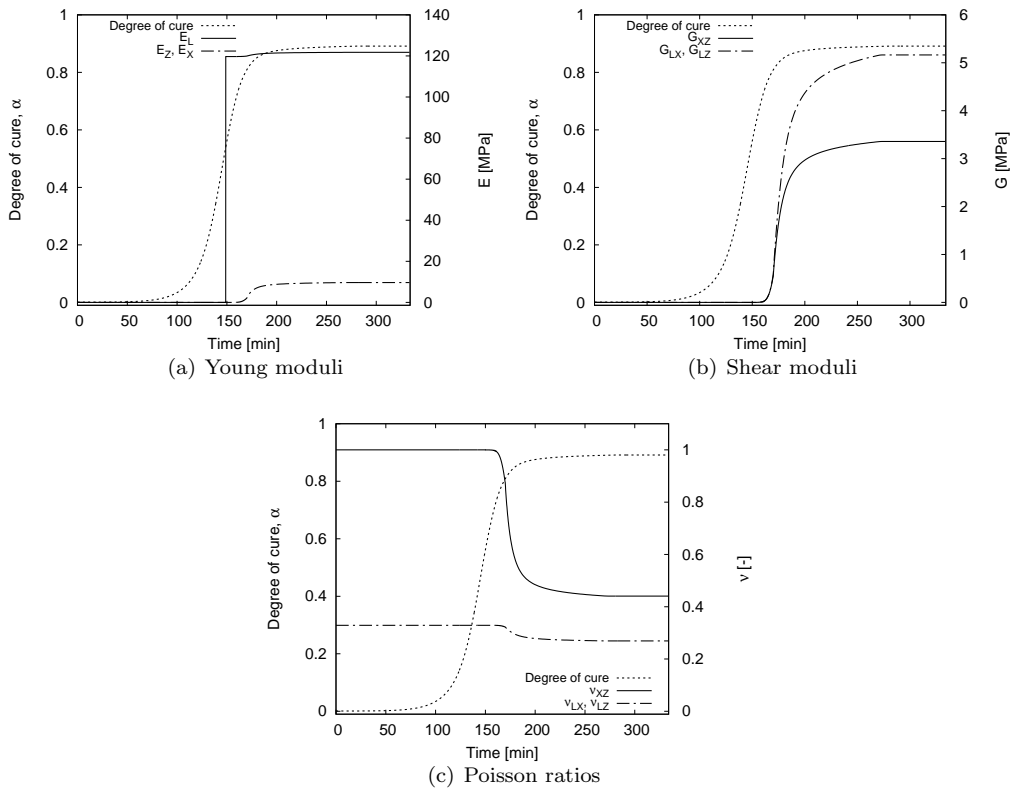


Figure 9: AS4/8552 material properties evolution during the curing process.

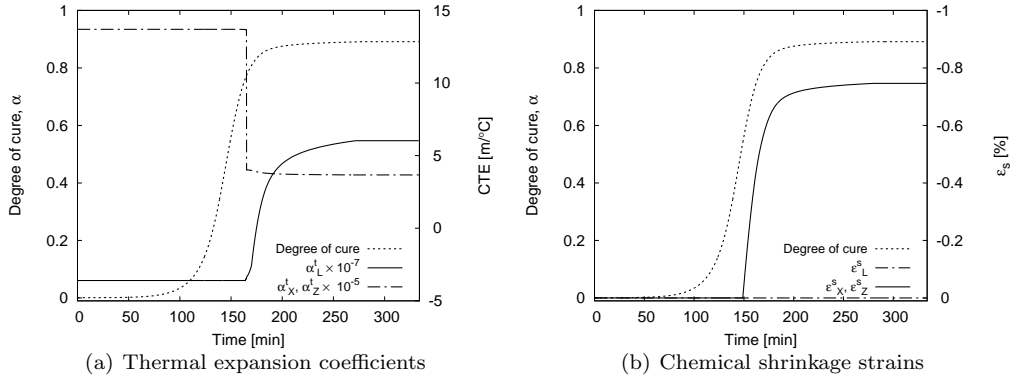


Figure 10: Loads evolution during the curing process.

## 5. Numerical results

The refined kinematic one-dimensional models introduced above have been used to investigate the process-induced deformations and residual stresses due to the curing process of an L-shaped composite structure. The present numerical approach has been initially validated using the closed-form solution presented by Takagaki *et al.* [37]. A convergence study has been carried out to investigate the performance of the numerical solution. The validated model has been subsequently used to evaluate the capability of the refined kinematic approximation to provide a high-fidelity description of the residual stresses and strain fields. The results obtained using different kinematic approximations have been compared to highlight the limitations and capabilities. Finally, the present approach has been compared with a full three-dimensional model to evaluate the accuracy of the current method and its efficiency.

### 5.1. Model description

This section describes the main features of the model considered. At first, the model is described from a physical point of view, followed by a detailed description of the numerical models. The geometry of the structure considered in the present analysis is shown in Fig. 11. The L-shaped composite panel has an angle of  $93^\circ$  between its two flanges. The panel has a stacking sequence of  $(90/0/90/0)_s$ , the lamination angle,  $\vartheta$ , is defined with respect to the  $z$ -axis. Fibers are parallel to the  $x$ -axis when the lamination angle is zero. On the other hand, a  $90^\circ$  lamination angle leads to fibers aligned to the  $y$ -axis. Each layer has a thickness equal to 0.19 mm. The coordinate  $x$  is a curvilinear coordinate which follows the panel curvature.

The tool material is Invar and has a Young's modulus equal to 150 GPa, a Poisson's ratio of

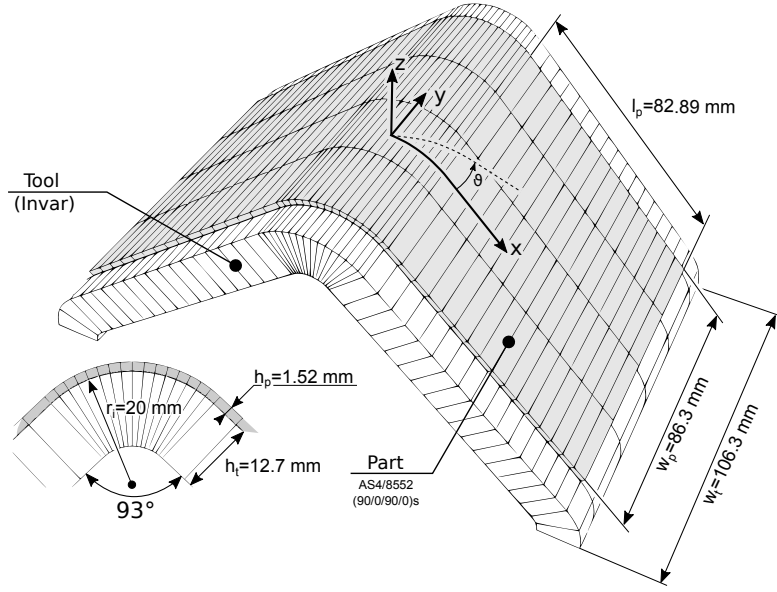


Figure 11: Geometry of the L-shaped panel .

0.28 and a thermal expansion coefficient of  $1.56 \times 10^{-6} / ^\circ C$ . The contact between the part and the tool is considered to be friction-less. The solution of the thermal problem, the evolution of the degree of cure, as well as the ply micromechanics, have not been the subject of this research and have instead been evaluated by means of the software RAVEN.

The FE model geometry is presented in Fig. 12. Since the structure has two symmetry planes and a cross-ply lamination, it is possible to consider only one-quarter of the structure by imposing the proper boundary conditions. In this case, three symmetry planes have been used. The results are expressed in the reference system shown in the figure.  $\varphi$  denotes the spring-in angle of the whole part, that is, it is twice of the angle obtained on one flange. The tool/part interface has been modeled using a shear layer with a reduced shear stiffness to minimize the in-plane interaction between the two components and to allow relative sliding in a frictionless manner. The FE model includes three quadratic beam elements, one in the lateral part, where only the tool is present and two in the portion where both the tool and the part are present. Different cross-sectional meshes have been considered, all of them can be denoted with three parameters:  $M_a, M_b$  and  $M_t$ .  $M_a$  and  $M_b$  are the number of elements along the curved part and the flange respectively.  $M_t$  is the number of elements used through the thickness of the composite part. The model meshes have been denoted with the notation  $M_a \times M_b \times M_t$ , e.g., a model with a mesh  $8 \times 16 \times 4$  has 8 elements in the curved part, 16 in the flange and 4 through-the-thickness.

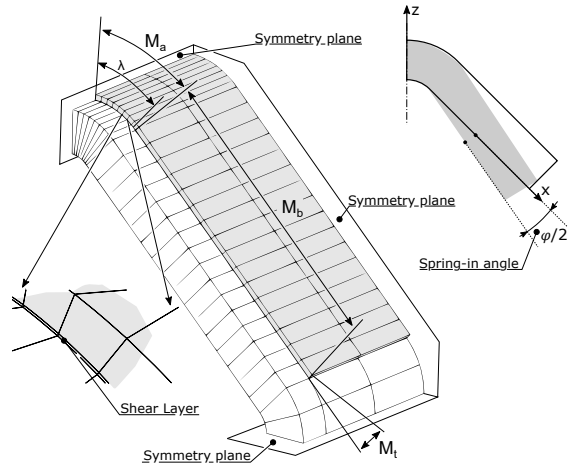


Figure 12: FE model details, reference system and boundary conditions.

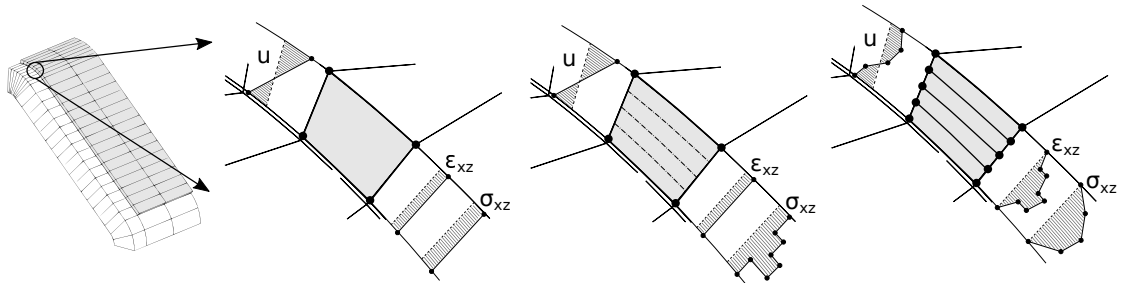


Figure 13: The three different modeling approaches and their corresponding displacements, shear strain and stress fields through the thickness. From the left: ELM, ESL and LW.

Three different cross-sectional kinematic approximations have been used in the present paper. Figure 13 shows the main features of each of these approaches.

The first method refers to a classical modeling approach. Independently from the cross-sectional mesh used, an equivalent material has been used for all the elements, and it is named Equivalent Laminate Model (ELM). The second approach, named Equivalent Single Layer (ESL) model, considers the material properties of each ply independently but a unique expansion, common to all layers and similarly to the first approach, is used to describe the kinematics through the thickness. The third approach, named Layer-Wise (LW), uses an independent kinematic description for each layer.

Whatever approach is used the kinematic model can be approximated using a different order of accuracy. Three Lagrange expansions have been used for the cross-sectional kinematic description, L4, L9 and L16, corresponding to linear, quadratic and cubic cross-sectional elements



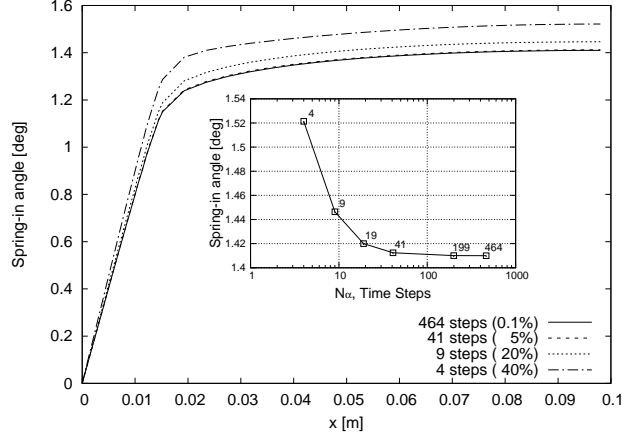


Figure 14: Closed-form solution for the spring-in angle along the plate length.

have been considered. Each model considered can thus be identified with a unique string, e.g., the model ESL-L9-8  $\times$  16  $\times$  1 is a model based on the ESL approach, the cross-sectional mesh is built using 9 node Lagrange elements and uses a mesh with 8 elements on the curved part, 16 along the flange and 1 through-thickness.

## 5.2. Model verification

The verification of the present model has been carried out using the closed-form solution proposed by Takagaki *et al.*[37] as a reference. The fulfillment of the assumptions on which the closed-form solution is based has required new constraints to be imposed on the present model. A plane strain condition is assumed and the tool is considered to be rigid. The constant value of the through-thickness shear strain has been ensured by using an ELM model with only one L4 element in the thickness direction, that is,  $M_t=1$  has been considered. Moreover, the closed-form solution assumes that the bending stiffness is affected mainly by carbon fibers and changes insignificantly during the curing process. Thus, the increment of the residual deformations at each time step is calculated considering the fully-cured bending stiffness of the panel and not the actual stiffness of the component at that degree of cure, as shown in Fig. 6.

The results from closed-form solution in terms of spring-in angle are shown in Fig. 14. A convergence analysis related to the number of time steps has been performed in order to define a suitable time discretization for the following analysis. The results show that a satisfactory convergence is achieved after 41 time steps. The number of steps stems from the choice of the maximum allowable variation in any material property, e.g., 5% of the final value.

Figures 15a and b show, respectively, the distribution of the spring-in angle and the shear

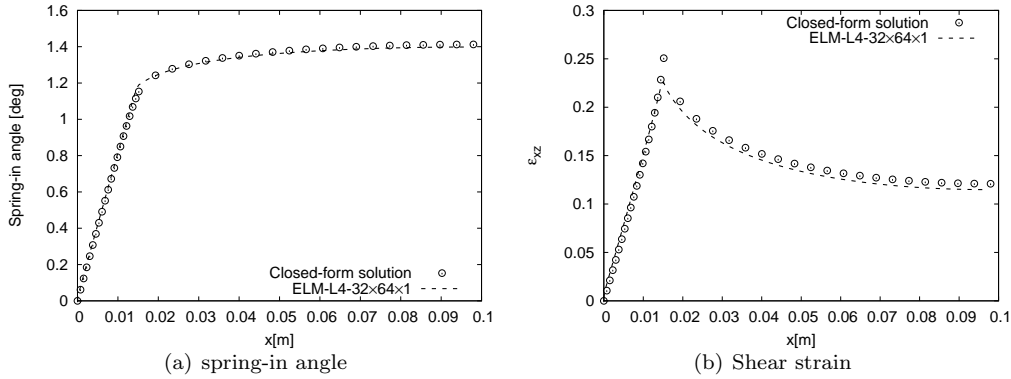


Figure 15: Comparison between the closed-form and the present ELM solutions.

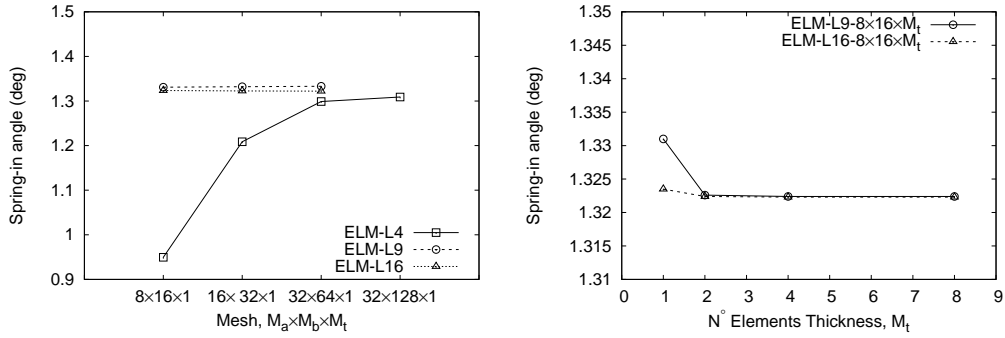
Model	DOFs	Spring-in angle [deg]
Closed-form	-	1.412
ELM*	6279	1.404
ELM	6279	1.318

\*Model updated with the closed-form solution assumptions.

Table 1: Spring-in angles evaluated by means of the closed-form solution and the present ELM.

strain along the length of the part as predicted by the closed form solution and the present numerical model. Table 1 reports the numerical value of the maximum spring-in angle evaluated using the closed-form solution and the present approach. When the assumptions of the closed-form solution are incorporated, the ELM model predictions accurately match the results obtained from the closed-form solution. When the real bending stiffness is considered for the tool removal simulation, the model predicts a lower spring-in angle, in this case, a reduction of the 6.1% can be observed. This effect can be explained by considering that the bending stiffness at the early stages of curing is lower than those at the end of the process. A lower stiffness produces weaker interaction forces at the tool/part interface, that is, a lower spring-in angle is obtained.

A convergence analysis has been performed to investigate the effects of various kinematic assumptions (models) through the cross-section. Figure 16a shows the results obtained considering a different number of elements along the curved part and the flange; linear, quadratic and cubic elements have been considered. The results show that the use of linear elements and a coarse mesh leads to an underestimation of the spring-in angle while quadratic and cubic elements provide accurate results for each mesh considered. The effect of the number of through-thickness elements is shown in Fig. 16b. Linear elements have not been considered because of their slow convergence. The use of higher-order polynomials, quadratic and cubic, makes the solution in-



(a) Number of elements on the curved part and flange (b) Number of elements through-the-thickness

Figure 16: Convergence analysis.

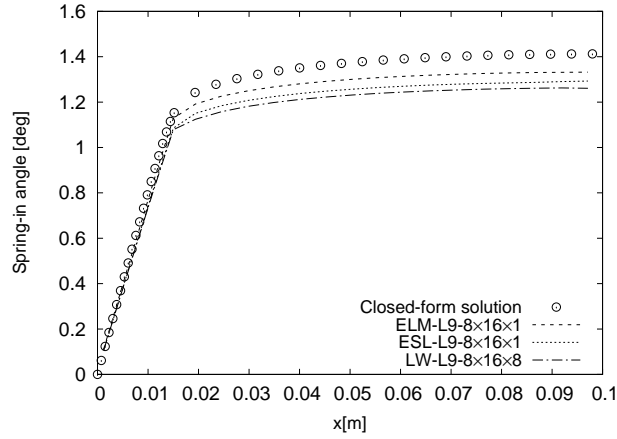


Figure 17: Spring-in angle distribution evaluated using different modeling approaches.

sensitive to the number of through-thickness elements and it can be shown that two elements are enough to ensure proper convergence.

### 5.3. High-fidelity through-thickness kinematic models

The use of high-fidelity through-thickness kinematic models has been investigated in this section. Equivalent Single Layer, ESL, and Layer-Wise, LW, models have been adopted and compared with the classical approach based on the ELM. All the models considered adopt L9 elements for the cross-sectional kinematic description. Figure 17 shows the spring-in angle distribution evaluated using all the models presented in the present paper. It can be observed that, when refined kinematic models are used, a lower spring-in angle is predicted. Table 2 reports the maximum value of spring-in angle and the degrees of freedom, DOFs, evaluated for each model

Model	DOFs	Spring-in Angle [deg]
Closed-form	-	1.412
ELM	6279	1.318
ESL	6279	1.293
LW	16569	1.261

Table 2: Spring-in angle and degrees of freedom of the models considered.

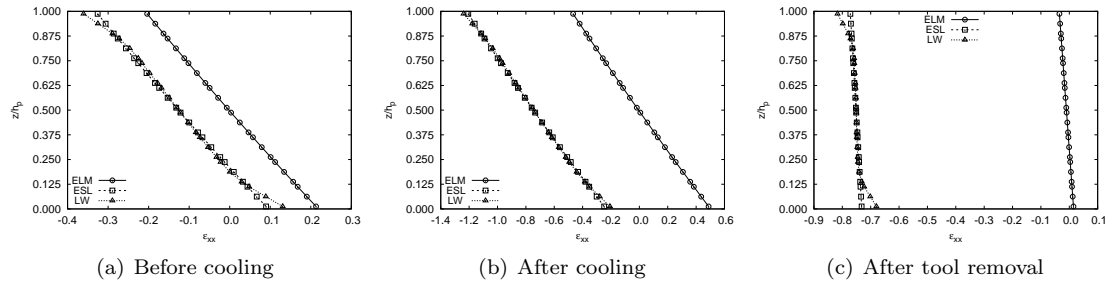


Figure 18: Through-thickness distribution of  $\varepsilon_{xx}$ .

considered. The use of an ESL model leads to a reduction of 1.9% in the value of the maximum deflection relative to the ELM. This effect can be traced back to the loads definition. Since the ELM assumes the material properties as the equivalent bending properties, see Fig. Appendix B, it ignores the in-plane thermal and shrinkage deformations. The use of an ESL model allows the real material properties to be considered for each ply, that is, the in-plane loads can be included. The LW model predicts a spring-in angle that is 2.5% lower than the angle predicted by the ESL model.

The convenience in the use of refined kinematic models can be further appreciated by the analysis of the residual stress and strain fields obtained using the different modeling approaches. Figures 18 and 19 show the through-thickness distribution of the axial,  $\varepsilon_{xx}$ , and transverse shear,  $\varepsilon_{xz}$ , strains. The results have been evaluated for an angle  $\lambda = 24.47^\circ$ , for the definition of  $\lambda$  see Fig. 12. Three different time steps, during the curing process, have been considered: (1) before the cooling, (2) after the cooling and (3) after the tool removal.

The normal strain has an almost linear distribution, see Fig. 18a. The shift between the ELM and the other approaches is due to the lack of the in-plane thermal and shrinkage deformations, this is confirmed by the effect of the cooling-down, see 18b, that increases this gap. The axial deformation is released during the tool removal, see 18c. The ELM predicts a null residual strain while the refined models are able to detect an almost constant residual strain due to the in-plane loads.

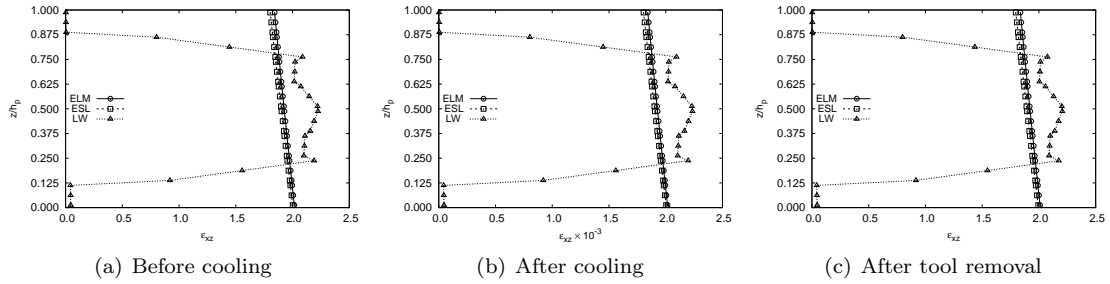


Figure 19: Through-thickness distribution of  $\varepsilon_{xz}$ .

The transverse shear deformation profile through the thickness is shown in Fig. 19. The distributions obtained using the ELM and ESL models have a linear behavior, a direct consequence of the quadratic formulation of the displacements field. The use of an LW model ensures a much more accurate description of the shear deformation. The LW model fulfills the zero shear strain conditions at the top and bottom of the laminate and predicts the discontinuities at the layer interfaces, as expected. The transverse shear strain originates in the first part of the curing process, just after the gelation point. At this curing stage, the low material stiffness does not produce any significant stress. When the vitrification takes place, the deformation is fixed, that is, neither the cooling process, Fig. 19b, and the demolding, Fig. 19c, modify the shear strain distribution.

Figures 20 and 21 show the in-plane and transverse shear stress distributions. The ELM predicts a linear distribution of the normal stress,  $\sigma_{xx}$ . When the tool is removed, see 20c, the normal stress is released giving way to the spring-in angle. The use of ESL or LW models leads to a completely different result. The in-plane thermal and shrinkage loads coupled with the stacking sequence produce a step-wise stress distribution with some layers in compression and others in traction, see 20a. The cooling down process increases the axial stress, see 20b, that is partially released during the tool removal. Significant residual stress, see 20c, can be observed in the final component.

The transverse shear stress distributions are shown in Fig. 21. The results emphasize the importance of the use of the LW approach when an accurate description of the transverse shear is required. Both the ELM and ESL are not able to fulfill the boundary conditions at the laminate top and bottom. Moreover, the use of a unique expansion for the whole laminate thickness leads to a discontinuous stress distribution. When an independent kinematic model for each layer is used, as in the case of the LW model, the results show null shear stress at the free surfaces, and

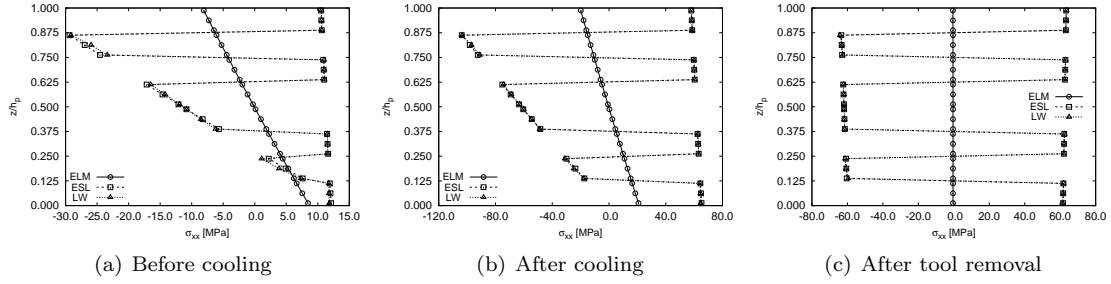


Figure 20: Through-thickness distribution of  $\sigma_{xx}$ .

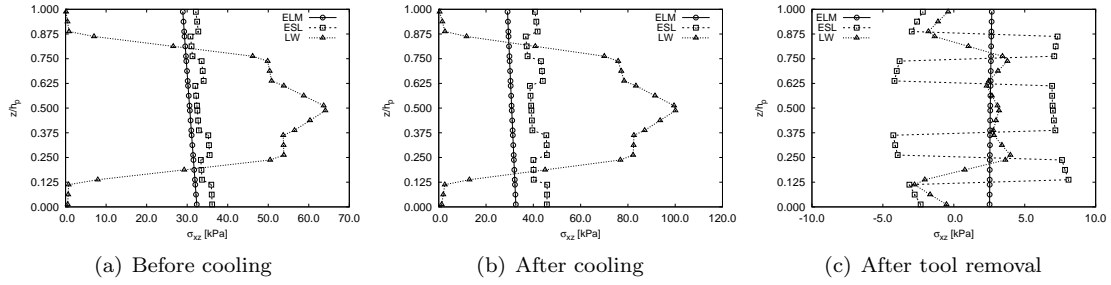


Figure 21: Through-thickness distribution of  $\sigma_{xz}$ .

the stress are fairly continuous at the layer interfaces.

Figure 22 shows the time evolution of the stresses and strains during the curing process. The normal stress and strain, see 22a, show a similar development. They have a first variation across the vitrification point but, 85% of their value is due to the cooling-down process, starting from  $t=240$  up to the end of the process. The transverse shear strain and stress, see 22b, follow two different time histories. The shear strain increases drastically during the early stages of the process up to the vitrification when the strain value becomes almost constant. The shear stress has a lag with respect to the shear strain, its value becomes significant after the vitrification point and then increases during the whole process.

#### 5.4. Comparison between LW and solid models

The results demonstrate that the refinement of the kinematic description may be used to increase the fidelity of the numerical model. LW model can predict complex residual stress fields that cannot be predicted using standard approaches. The present section aims to confirm the accuracy of the present one-dimensional LW model by comparing the results with those from two full three-dimensional models. The first model has been built using linear brick elements, 8 nodes solid elements, and has been named 3D-H8. The second model uses quadratic brick

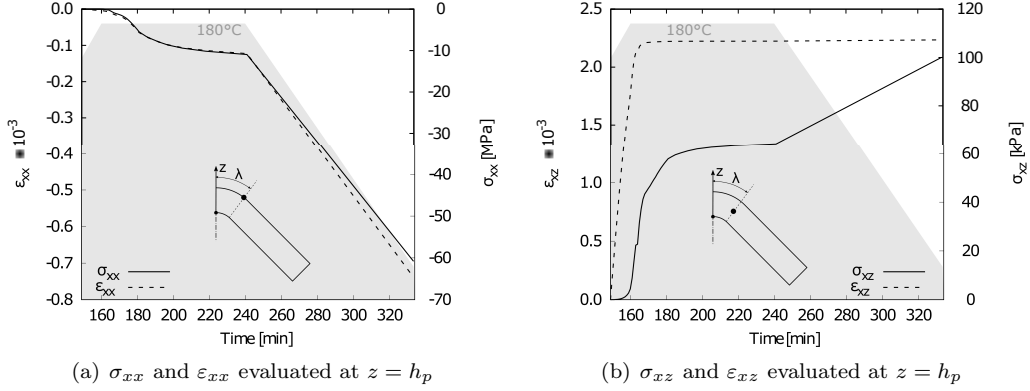


Figure 22: Stress and strain time evolution at  $\lambda = 40.78^\circ$ , the shadowed area shows the curing cycle.

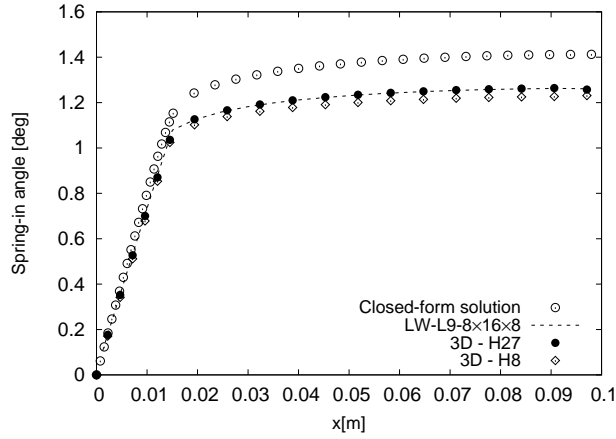


Figure 23: Spring-in angle distribution evaluated using the present LW and three-dimensional models.

elements with 27 nodes and is denoted as 3D-H27. Both models use 3 elements through the thickness of each layer. Since solid elements are prone to numerical issues when high aspect ratios are considered, the choice of 3 elements per layer necessitates a mesh refinement in all the other directions. A trade-off between numerical accuracy and computational cost has been found for a limit value of the aspect ratio equal to 30, since each layer is 0.19 mm thick, each element cannot have in-plane side length greater than 1.9 mm.

Figure 23 shows the spring-in angle evaluated using the present one-dimensional model and the full three-dimensional approach. The results obtained using the present one-dimensional model match with those from the 3D-H27 model while the solid model based on linear brick elements underestimates the spring-in angle.

The through-thickness residual stress distributions evaluated with the different approaches

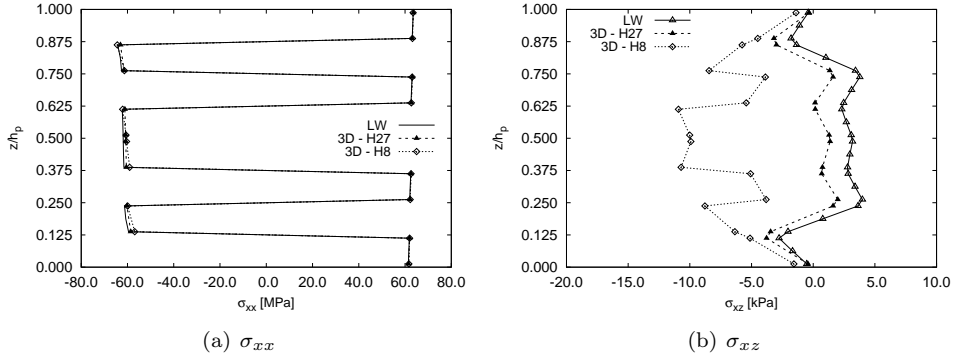


Figure 24: Through-thickness residual stress distributions, LW vs solid.

Model	DOFs	Spring-in Angle [deg]	$\Delta\%$
Closed-form	-	1.412	12.33
ELM	6279	1.318	4.85
ESL	6279	1.293	2.86
LW	16569	1.261	0.32
3D-H8	226956	1.245	-0.95
3D-H27	599571	1.257	0.00

Table 3: Computational cost and accuracy of the models considered.

are shown in Fig. 24.

When the normal stress,  $\sigma_{xx}$ , is considered, the three-dimensional solutions are in agreement with the results of the present one-dimensional approach. The use of a linear kinematic model, 3D-H8, leads to an inaccurate shear stress distribution, even if a mesh with three elements per layer has been used. Figure 24b shows a substantial agreement between the present LW model and the 3D-H27.

Table 3 reports the maximum value of the spring-in angle evaluated with different approaches. The second column indicates the number of degrees of freedom, DOFs, required by the model. The last column shows the percentage difference,  $\Delta\%$ , in the spring-in angle with respect to the 3D-H27, that has been considered as the reference.

The present LW model provides an error lower than 0.5% with respect to the reference model. At the same time, the number of degrees of freedom highlight the high computational efficiency of the present approach. In fact, the LW model requires only 2.7% of the number of DOFs needed by the 3D-H27 model.

Figure 25 compares the performances of the models considered with respect to the reference solution, the 3D-H27. For each model the results reported consist of the accuracy,  $\Delta\%$ , the



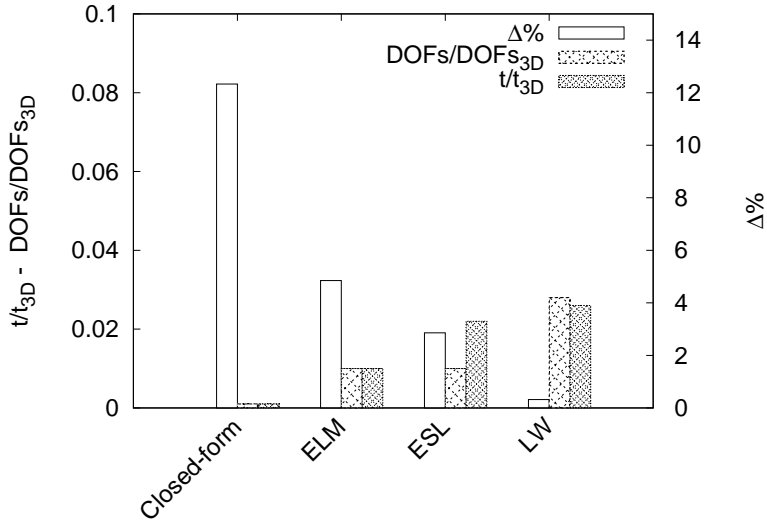


Figure 25: Computational cost and accuracy of the present models with respect to the reference solution

number of DOFs and the solution time normalized with respect to the corresponding values for the 3D solid model,  $DOFs/DOFs_{3D}$  and  $t/t_{3D}$ , respectively.

The closed-form solution has a negligible computational cost but cannot ensure reliable results. The use of ELM and ESL models can reduce the error in terms of spring-in angle. They both have the same number of DOFs since they are based on the same kinematic model. However, the ESL model is more time consuming since the integration procedure requires to consider each layer as an independent domain. The use of the LW model ensures a very accurate result but at a higher computational cost. Even if the LW model requires a higher number of DOFs relative to the ELS, the computational costs are comparable since the solution time of the linear problem, driven by the DOFs, is negligible with respect to the time spent for the numerical integrations, that depends on the number of layers in which the cross-section is subdivided.

### 5.5. Quasi-isotropic laminate

The last numerical example considers a quasi-isotropic laminate. The same approach presented in the previous sections was adopted and the same geometry, see Figure 11, considered. The new stacking sequence is  $(90/45/0/-45)_s$ ; each lamina has AS4/8552, and the curing cycle is the one of Section 4. A layer-wise formulation has been considered to have an accurate residual stress field description. Although the lamination is symmetric and balanced, no symmetry conditions were used, given that the angled layers may lead to non-symmetric deformations. The complete model has 59427 DOFs.

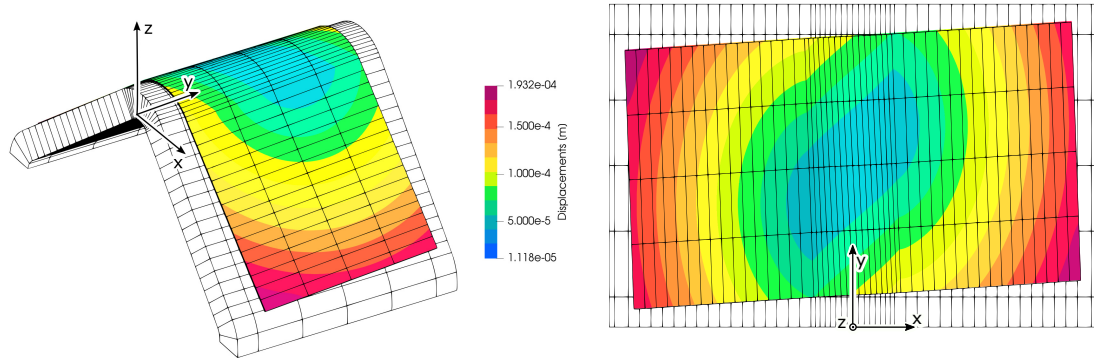


Figure 26: Displacement field of the composite component at the end of the cooling-down phase, before to be removed from the tool. Three-dimensional view on the left, top view on the right. Magnification factor  $\times 30$ .

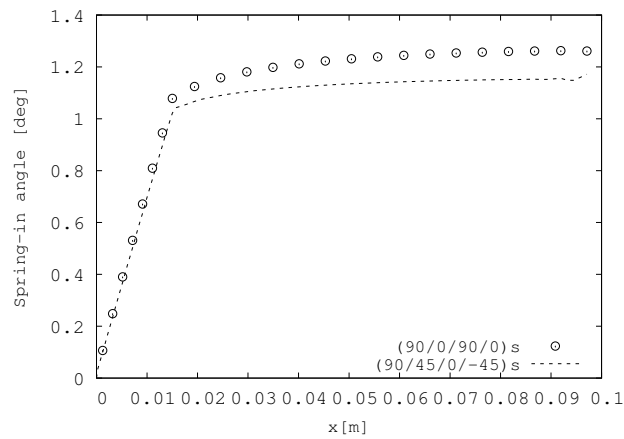


Figure 27: Spring-in angle for the cross-ply and quasi-isotropic laminates.

Figure 26 shows the displacement field of the composite component before the tool removal. As expected, the deformation is no longer symmetric because of the effects of the  $\pm 45^\circ$  layers. The spring-in angle evaluated in the central section of the composite part is reported in Fig. 27. The quasi-isotropic laminate shows a lower residual deformation probably due to the lower bending stiffness generated by the angled layers and resulting in lower interface forces, and, in turn, a reduced spring-in angle. However, the difference in the maximum angle and the free tip is quite low. Figure 28 reports the residual stress fields. The normal stress, Figure 28a, shows reduced stress gaps between the layers. Figure 28b reports the residual transverse shear stress. Figure 29 shows the cross-sectional deformation of three different points of the component. Point B is located at the component mid-span while points A and C at the two edges. The undeformed

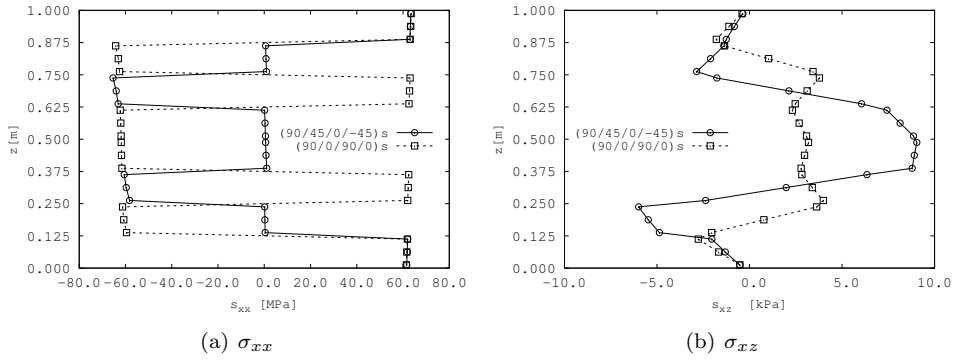


Figure 28: Through-thickness residual stress distributions, cross-ply and quasi-isotropic.

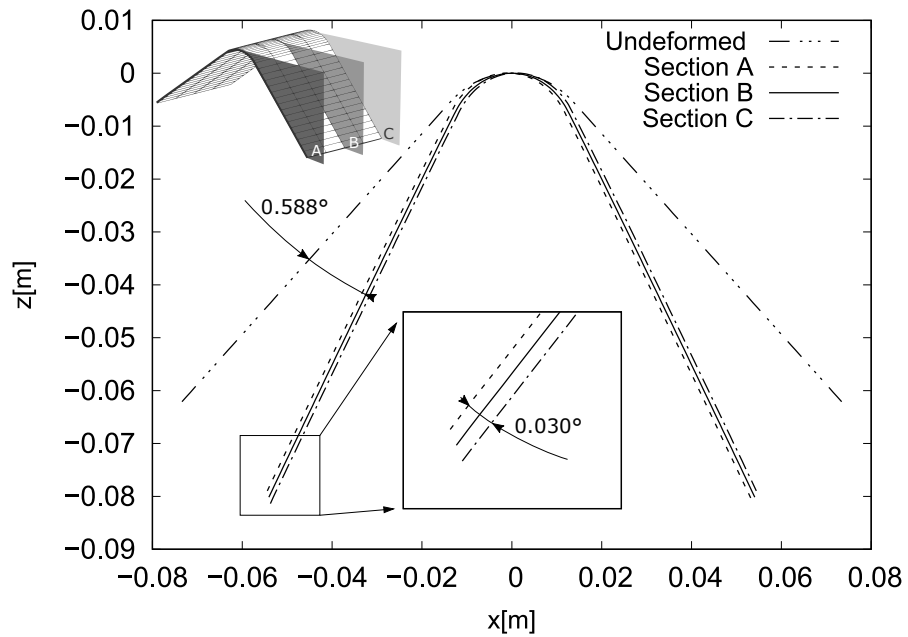


Figure 29: Cross-sectional deformation, point B is located at the component mid-span while point A and C at the two edges. Magnification factor  $\times 30$ .

cross-section is reported as well. The spring-in angle is the difference between the undeformed and the deformed flanges; a value of  $2 \times 0.588^\circ$  is obtained in the central section. It is worth to notice that the warping of the component shown in Figure 26, leads to torsion. A rotation of  $0.03^\circ$  originates between section A and section C that, considering the component length, corresponds to a torsional gradient of  $0.352^\circ/m$ .

## 6. Conclusions

A computationally efficient modeling approach has been presented for the accurate evaluation of process-induced deformations and residual stresses in composite parts. The material curing process has been evaluated by means of the software RAVEN. The evolution of the mechanical properties as a function of the degree of cure, have been exploited to simulate the curing process using a cure hardening instantaneously linear elastic (CHILE) constitutive model. The use of refined one-dimensional kinematic models and the capabilities of the Carrera Unified Formulation have been exploited to solve the problem with different accuracy levels. The capability of these models to deal with accurate through-thickness deformations has made it possible to predict the complex stress fields stemming from the curing process. A benchmark example based on an L-shaped composite component undergoing curing has been selected to compare the results obtained using different computational approaches. A closed-form solution, the present refined one-dimensional models and classical solid models, have been considered. The synergistic use of these tools has led to a comprehensive understanding of the advantages and limitations of the different modeling approaches considered. The following are some relevant conclusions that can be drawn from this study:

- The use of a closed-form solution for the evaluation of the process-induced deformation, here identified with the spring-in angle, can lead to a qualitative result. More refined approaches are required to reduce the error. The results show that an Equivalent Laminate Model can lead to an error lower than 5% with respect to a full three-dimensional solution.
- The prediction of accurate residual stress fields requires the fidelity of the model to be increased. The normal stresses can be predicted with an Equivalent Single Layer model. A layer-wise approach is mandatory when accurate prediction of the transverse shear stress field is required.
- The use of the present modeling approach can lead to a dramatic reduction of the computational costs. The accuracy of the Layer-Wise model has been proved by the perfect

matching of the results with those from the solid model. At the same time the LW model requires only 2.3% of the DOFs used in the solid model.

- Based on the results obtained, the use of a through-thickness linear kinematic model is not recommended, regardless of the model adopted, since it would lead to a significant error in the shear description, and consequently, the process-induced deformations.
- The present approach can be used to investigate general stacking-sequences and predict complex residual deformations, as shown by the analysis of a quasi-isotropic laminate, where a torsion of the component appeared.

Future works could deal with more complex configurations and the analysis of the relevance of the material parameters on the determination of the spring-in angle and the residual stress. It may be of interest to the identification of a subset of the nine parameters having a significant role and, thus, avoid determining the unnecessary ones. Regarding this aspect, some guidelines can be provided based on the numerical results of the present paper. The out-of-plane properties are fundamental to determine the deformed state of the part. On the other hand, the in-plane ones are crucial for the residual stress, and, if the transverse shear stress is of interest, both sets of properties must be carefully handled.

## 7. Acknowledgments

This research work has been carried out within the Joint Project for the Internationalization of Research between the Politecnico di Torino and University of British Columbia.

## Appendix A. Nomenclature

### Nomenclature

$\mathbf{K}$  Total stiffness matrix at the  $i$ -th time step, [Nm]

$\alpha$  Degree of cure, [-]

$\alpha_g$  Gelation degree of curing [-]

$\mathbf{F}$  Force vector, [N]

$\beta$  Thermal expansion coefficients

$\sigma$  Stresses vector , [Pa]  
 $\varepsilon$  Strains vector, [-]  
 $C$  Material coefficients matrix, [Pa]  
 $D$  Differential operator, [-]  
 $u$  Displacements vector, [m]  
 $u_\tau$  Axial unknowns  
 $u_{i\tau}$  Nodal displacements  
 $\Delta$  Increment during a simulation step, [-]  
 $\delta$  Virtual Variation  
 $\sigma$  Stresses vector, [Pa]  
 $\square^i$  Quantity evaluated at the  $i$ -th time step, [-]  
 $\square_p$  Value associated to the composite part, [-]  
 $\square_{sl}$  Value associated to the shear layer, [-]  
 $\square_{tr}$  Value associated to the tool removal phase, [-]  
 $\square_t$  Value associated to the tool, [-]  
 $\mathbf{f}^{js}$  Load vector fundamental nucleus  
 $\mathbf{k}^{ij\tau s}$  Stiffness Matrix fundamental nucleus  
 $\varepsilon$  Strains vector, [-]  
 $\varepsilon_s^i$   $i$ -th shrinkage strain variation [%]  
 $\varepsilon_T^i$   $i$ -th thermal strain variation [%]  
 $\varphi$  Spring-in angle, [deg]  
 $\vartheta$  Lamination angle, [deg]  
 $E^i, G^i, \nu^i$  Material Properties at the  $i$ -th time step

$F_\tau, F_s$  Generic cross-sectional functions expansion

$L_\tau, L_s$  Cross-sectional Lagrange polynomial

$L_{ext}$  External work

$L_{int}$  Internal work

$M$  Number of terms in the functions expansion

$M_a, M_b, M_t$  Mesh parameters

$N_\alpha$  Number of time/curing steps [-]

$N_i, N_j$  FEM shape functions

$N_n$  Number of nodes of the element

$T$  Temperature [ $^{\circ}C$ ]

$t$  Time, [s]

$T_g$  Gelation temperature [ $^{\circ}C$ ]

$u_x, u_y, u_z$  Displacement components, [m]

## Appendix B. Material properties

Table B.4 shows the carbon/epoxy properties in the material reference system where  $L$  denotes the fiber direction while  $Z$  and  $X$  the through-the-thickness and the transverse direction respectively. The value of the chemical shrinkage in the fiber direction is assumed to be equal to zero. The equivalent laminate properties can be obtained from those of the lamina. The equivalent elastic modulus is defined as:

$$E^{eq} = \frac{\int_{-h/2}^{h/2} E(z)z^2 dz}{\int_{-h/2}^{h/2} z^2 dz} \quad (\text{B.1})$$

T	t	$\alpha$	$E_L$	$E_Z, E_X$	$\nu_{LX,LZ}$	$\nu_{XZ}$	$G_{LX,LZ}$	$G_{XZ}$	$\alpha_L^t \times 10^{-7}$	$\alpha_{Z,X}^t \times 10^{-5}$	$\epsilon_{X,Z}^s$
[s]	[°C]	[-]	[Gpa]	[Mpa]	[-]	[-]	[Mpa]	[Mpa]	[m/°C]	[m/°C]	[%]
148.88	168.88	0.54	119.70	0.25	0.329	1.000	0.06	0.06	-3.600	13.699	0.000
149.77	169.77	0.56	119.70	0.41	0.329	1.000	0.10	0.10	-3.599	13.699	-0.036
150.68	170.68	0.57	119.70	0.68	0.329	1.000	0.17	0.17	-3.599	13.699	-0.072
151.60	171.60	0.59	119.70	1.13	0.329	1.000	0.28	0.28	-3.598	13.699	-0.107
152.55	172.55	0.61	119.70	1.88	0.329	1.000	0.47	0.47	-3.597	13.699	-0.143
153.54	173.54	0.62	119.70	3.14	0.329	1.000	0.79	0.79	-3.595	13.699	-0.179
154.55	174.55	0.64	119.70	5.24	0.329	1.000	1.31	1.31	-3.592	13.699	-0.214
155.61	175.61	0.66	119.70	8.74	0.329	0.999	2.19	2.19	-3.587	13.699	-0.250
156.71	176.71	0.67	119.70	14.56	0.329	0.999	3.64	3.64	-3.578	13.698	-0.286
157.86	177.86	0.69	119.70	24.20	0.329	0.998	6.06	6.06	-3.563	13.698	-0.321
159.07	179.07	0.71	119.70	40.10	0.329	0.998	10.05	10.04	-3.538	13.697	-0.357
160.38	180.00	0.72	119.71	70.38	0.329	0.996	17.68	17.63	-3.491	13.695	-0.393
161.87	180.00	0.74	119.71	144.62	0.329	0.991	36.50	36.32	-3.375	13.691	-0.430
163.57	180.00	0.76	119.73	297.41	0.328	0.981	75.80	75.05	-3.133	13.682	-0.467
165.06	180.00	0.77	119.75	517.61	0.327	0.968	133.86	131.52	-2.775	13.669	-0.496
165.15	180.00	0.77	119.75	534.66	0.327	0.967	138.42	135.92	-3.361	4.015	-0.498
167.06	180.00	0.79	119.80	983.09	0.326	0.939	262.28	253.51	-3.146	4.007	-0.530
168.42	180.00	0.80	119.85	1429.67	0.324	0.911	393.25	373.98	-2.919	3.999	-0.550
169.53	180.00	0.81	119.90	1878.20	0.323	0.884	533.06	498.49	-2.674	3.990	-0.565
170.19	180.00	0.81	119.96	2305.49	0.321	0.858	674.56	620.50	-2.426	3.981	-0.574
170.60	180.00	0.81	120.01	2706.08	0.320	0.833	815.13	738.00	-2.178	3.972	-0.579
171.03	180.00	0.81	120.06	3083.65	0.318	0.811	955.12	851.59	-1.930	3.963	-0.584
171.46	180.00	0.82	120.12	3440.43	0.316	0.789	1094.55	961.54	-1.683	3.954	-0.589
172.06	180.00	0.82	120.19	3887.14	0.314	0.762	1279.56	1102.88	-1.352	3.942	-0.595
172.69	180.00	0.82	120.26	4304.35	0.312	0.737	1463.56	1238.70	-1.022	3.930	-0.602
173.35	180.00	0.83	120.33	4695.22	0.310	0.714	1646.47	1369.38	-0.691	3.918	-0.609
174.21	180.00	0.83	120.42	5150.74	0.308	0.688	1873.36	1525.99	-0.279	3.902	-0.617
175.15	180.00	0.83	120.51	5574.37	0.305	0.663	2098.55	1675.92	0.133	3.887	-0.626
176.16	180.00	0.84	120.59	5969.98	0.302	0.640	2321.98	1819.75	0.545	3.872	-0.634
177.26	180.00	0.84	120.68	6340.76	0.300	0.619	2543.59	1957.98	0.956	3.857	-0.642
178.48	180.00	0.85	120.77	6689.40	0.297	0.600	2763.29	2091.03	1.366	3.842	-0.651
179.85	180.00	0.85	120.85	7018.16	0.295	0.581	2981.00	2219.27	1.776	3.827	-0.659
181.42	180.00	0.85	120.94	7328.93	0.292	0.564	3196.60	2343.00	2.184	3.812	-0.667
183.25	180.00	0.86	121.03	7623.34	0.290	0.548	3409.94	2462.50	2.590	3.797	-0.675
185.43	180.00	0.86	121.11	7902.79	0.287	0.533	3620.89	2577.98	2.994	3.783	-0.684
188.13	180.00	0.87	121.20	8168.50	0.285	0.518	3829.33	2689.67	3.396	3.768	-0.692
192.38	180.00	0.87	121.30	8470.74	0.282	0.502	4075.98	2818.94	3.875	3.750	-0.701
198.39	180.00	0.87	121.40	8756.48	0.279	0.487	4318.74	2943.36	4.350	3.733	-0.711
207.42	180.00	0.88	121.50	9027.26	0.276	0.473	4557.58	3063.23	4.820	3.716	-0.720
221.36	180.00	0.88	121.59	9276.55	0.274	0.461	4785.13	3175.29	5.271	3.699	-0.730
247.36	180.00	0.89	121.69	9531.48	0.271	0.448	5025.57	3291.57	5.751	3.682	-0.739
333.33	20.00	0.89	121.75	9674.51	0.269	0.441	5163.91	3357.54	6.029	3.672	-0.746

Table B.4: AS4/8552 material properties evolution during the curing process.



The equivalent shear modulus is defined as:

$$G^{eq} = \frac{\int_{-h/2}^{h/2} G(z) dz}{\int_{-h/2}^{h/2} dz} \quad (\text{B.2})$$

The equivalent through-the-thickness normal strain can be written as:

$$\varepsilon_Z^{eq} = \varepsilon_Z^s + \nu_{XZ}\varepsilon_X^s + \nu_{LZ}\varepsilon_L^s + \varepsilon_Z^t + \nu_{XZ}\varepsilon_X^t + \nu_{LZ}\varepsilon_L^t \quad (\text{B.3})$$

The thermal strains can be expressed in terms of the thermal expansion coefficients as:

$$\varepsilon_Z^{eq} = \varepsilon_Z^s + \nu_{XZ}\varepsilon_X^s + \nu_{LZ}\varepsilon_L^s + \alpha_Z^t \Delta T + \nu_{XZ}\alpha_X^t \Delta T + \nu_{LZ}\alpha_L^t \Delta T \quad (\text{B.4})$$

## References

- [1] G. Fernlund, C. Mobuchon, N. Zobeiry, 2.3 autoclave processing, in: B. P.W.R., Z. C.H. (Eds.), *Comprehensive Composite Materials II*, Elsevier, 2018, Ch. 2, pp. 42–62.
- [2] N. Zobeiry, A. Poursartip, The origins of residual stress and its evaluation in composite materials, in: S. S. Beaumont P.W.R., H. A. (Eds.), *Structural integrity and durability of advanced composites*, Elsevier, 2015, pp. 43–72.
- [3] G. Twigg, A. Poursartip, G. Fernlund, Tool–part interaction in composites processing. part i: experimental investigation and analytical model, *Composites Part A: Applied Science and Manufacturing* 35 (1) (2004) 121–133.
- [4] G. Twigg, A. Poursartip, G. Fernlund, Tool–part interaction in composites processing. part ii: numerical modelling, *Composites Part A: Applied Science and Manufacturing* 35 (1) (2004) 135–141.
- [5] C. Albert, G. Fernlund, Spring-in and warpage of angled composite laminates, *Composites Science and Technology* 62 (14) (2002) 1895–1912.
- [6] G. Fernlund, N. Rahman, R. Courdji, M. Bresslauer, A. Poursartip, K. Willden, K. Nelson, Experimental and numerical study of the effect of cure cycle, tool surface, geometry, and lay-up on the dimensional fidelity of autoclave-processed composite parts, *Composites part A: applied science and manufacturing* 33 (3) (2002) 341–351.

- [7] G. Fernlund, A. Osooly, A. Poursartip, R. Vaziri, R. Courdji, K. Nelson, P. George, L. Hendrickson, J. Griffith, Finite element based prediction of process-induced deformation of autoclaved composite structures using 2d process analysis and 3d structural analysis, *Composite Structures* 62 (2) (2003) 223–234.
- [8] K. Priesnitz, J. Sinke, R. Benedictus, On the simulation of panel distortions due to hot curing adhesives, *International Journal of Solids and Structures* 51 (13) (2014) 2470 – 2478. doi:<https://doi.org/10.1016/j.ijsolstr.2014.03.016>.
- [9] E. Kappel, D. Stefaniak, G. Fernlund, Predicting process-induced distortions in composite manufacturing—a pheno-numerical simulation strategy, *Composite Structures* 120 (2015) 98–106.
- [10] R. H. Nelson, D. S. Cairns, Prediction of dimensional changes in composite laminates during cure, *Tomorrow's Materials: Today*. 34 (1989) 2397–2410.
- [11] D. Radford, R. Diefendorf, Shape instabilities in composites resulting from laminate anisotropy, *Journal of Reinforced Plastics and Composites* 12 (1) (1993) 58–75.
- [12] M. R. Wisnom, K. D. Potter, N. Ersoy, Shear-lag analysis of the effect of thickness on spring-in of curved composites, *Journal of composite Materials* 41 (11) (2007) 1311–1324.
- [13] A. R. A. Arafath, R. Vaziri, A. Poursartip, Closed-form solution for process-induced stresses and deformation of a composite part cured on a solid tool: Part ii—curved geometries, *Composites Part A: Applied Science and Manufacturing* 40 (10) (2009) 1545–1557.
- [14] A. Johnston, R. Vaziri, A. Poursartip, A plane strain model for process-induced deformation of laminated composite structures, *Journal of Composite Materials* 35 (16) (2001) 1435–1469. doi:10.1106/YXEA-5MH9-76J5-BACK.
- [15] K. Takagaki, S. Minakuchi, N. Takeda, Process-induced strain and distortion in curved composites. part i: Development of fiber-optic strain monitoring technique and analytical methods, *Composites Part A: Applied Science and Manufacturing* 103 (2017) 236–251.
- [16] K. Takagaki, S. Minakuchi, N. Takeda, Process-induced strain and distortion in curved composites. part ii: Parametric study and application, *Composites Part A: Applied Science and Manufacturing* 103 (2017) 219–229.

- [17] A. Ding, J. Wang, A. Ni, S. Li, A new analytical solution for cure-induced spring-in of L-shaped composite parts, *Composites Science and Technology* 171 (2019) 1 – 12. doi:  
<https://doi.org/10.1016/j.compscitech.2018.12.004>.
- [18] Convergent Manufacturing Technologies, Compro simulation software.  
URL <http://www.convergent.ca/products/compro-simulation-software>
- [19] N. Zobeiry, A. Forghani, C. Li, K. Gordnian, R. Thorpe, R. Vaziri, G. Fernlund, A. Poursartip, Multiscale characterization and representation of composite materials during processing, *Philosophical Transactions of the Royal Society A: Mathematical, Physical and Engineering Sciences* 374 (2071) (2016) 20150278.
- [20] G. Fernlund, A. Floyd, M. Shewfelt, M. Hudek, Process analysis and tool compensation for a complex composite panel, in: 22nd Annual Technical Conference, Seattle, 2007.
- [21] N. Ersoy, T. Garstka, K. Potter, M. R. Wisnom, D. Porter, G. Stringer, Modelling of the spring-in phenomenon in curved parts made of a thermosetting composite, *Composites Part A: Applied Science and Manufacturing* 41 (3) (2010) 410 – 418. doi:<https://doi.org/10.1016/j.compositesa.2009.11.008>.
- [22] N. Ersoy, T. Garstka, K. Potter, M. R. Wisnom, D. Porter, M. Clegg, G. Stringer, Development of the properties of a carbon fibre reinforced thermosetting composite through cure, *Composites Part A: Applied Science and Manufacturing* 41 (3) (2010) 401 – 409. doi:<https://doi.org/10.1016/j.compositesa.2009.11.007>.
- [23] W. Chen, D. Zhang, Improved prediction of residual stress induced warpage in thermoset composites using a multiscale thermo-viscoelastic processing model, *Composites Part A: Applied Science and Manufacturing* 126 (2019) 105 – 575. doi:<https://doi.org/10.1016/j.compositesa.2019.105575>.
- [24] L. Mezeix, A. Seman, M. Nasir, Y. Aminanda, A. Rivai, B. Castanié, P. Olivier, K. Ali, Spring-back simulation of unidirectional carbon/epoxy flat laminate composite manufactured through autoclave process, *Composite Structures* 124 (2015) 196 – 205. doi:<https://doi.org/10.1016/j.compstruct.2015.01.005>.
- [25] M. Fiorina, A. Seman, B. Castanie, K. Ali, C. Schwob, L. Mezeix, Spring-in prediction for carbon/epoxy aerospace composite structure, *Composite Structures* 168 (2017) 739 – 745. doi:<https://doi.org/10.1016/j.compstruct.2017.02.074>.

- [26] A. Ding, S. Li, J. Wang, A. Ni, L. Sun, L. Chang, Prediction of process-induced distortions in L-shaped composite profiles using path-dependent constitutive law, *Appl Compos Mater* 23 (2016) 1027–1045. doi:10.1007/s10443-016-9501-8.
- [27] X. Wang, Y. Zhao, H. Su, Y. Jia, Curing process-induced internal stress and deformation of fiber reinforced resin matrix composites: Numerical comparison between elastic and viscoelastic models, *Polymers and Polymer Composites* 24 (2) (2016) 155–160. doi:10.1177/096739111602400211.
- [28] E. Carrera, M. Petrolo, Refined beam elements with only displacement variables and plate/shell capabilities, *Meccanica* 47 (3) (2012) 537–556. doi:10.1007/s11012-011-9466-5.
- [29] E. Carrera, M. Petrolo, E. Zappino, Performance of cuf approach to analyze the structural behavior of slender bodies, *Journal of Structural Engineering* 138 (2) (2012) 285–297. doi:10.1061/(ASCE)ST.1943-541X.0000402.
- [30] E. Carrera, M. Cinefra, M. Petrolo, E. Zappino, *Finite Element Analysis of Structures Through Unified Formulation*, John Wiley & Sons, 2014.
- [31] Convergent Manufacturing Technologies, Raven simulation software.  
URL <http://www.convergent.ca/products/raven-simulation-software>
- [32] Hexcel, Hexply 8552 product data sheet, 2016.  
URL [http://www.hexcel.com/user\\_area/content\\_media/raw/HexPly\\_8552\\_us\\_DataSheet.pdf](http://www.hexcel.com/user_area/content_media/raw/HexPly_8552_us_DataSheet.pdf)
- [33] Hexcel, Hextow as4 product data sheet.  
URL [http://www.hexcel.com/user\\_area/content\\_media/raw/AS4\\_HexTow\\_DataSheet.pdf](http://www.hexcel.com/user_area/content_media/raw/AS4_HexTow_DataSheet.pdf)
- [34] D. Van Ee, A. Poursartip, Hexply 8552 material properties database for use with comprocca and raven, National Center for Advanced Materials Performance, Wichita, KS (2009).
- [35] A. Shahkarami, D. Van Ee, A. Poursartip, Material characterization for processing: Hexcel 8552, National Center for Advanced Materials Performance, Wichita, KS (2009).

- [36] C. Mobuchon, N. Zobeiry, C. Duffner, A. Poursartip, A multifaceted approach for process characterization of polymer-matrix composites, Proc. 12th Joint Canada-Japan/2nd Joint Canada-Japan-Vietnam Workshop on Composites, Takayama, Japan (2018).
- [37] K. Takagaki, S. Minakuchi, N. Takeda, Process-induced strain and distortion in curved composites. part i: Development of fiber-optic strain monitoring technique and analytical methods, Composites Part A: Applied Science and Manufacturing 103 (2017) 236 – 251. doi:<https://doi.org/10.1016/j.compositesa.2017.09.020>.